

Tuning Nanopore Structure of Hard Carbon Anodes by Zinc Gluconate for High Capacity Sodium Ion Batteries

Zongliang Zhang,^[a] Guanjie Li,^[b] Gemeng Liang,^[b] Pei Zhao,^[a] Xuerong Gong,^[a] Jiaxin Dai,^[a] Hesen Xiong,^[a] Zonghan Zhang,^[a] Jianfeng Mao,^[b] Shilin Zhang,^{*[b]} and Baofeng Wang^{*[a]}

Hard carbon serves as a highly promising anode material for sodium-ion batteries due to its stable structure and cost-effectiveness. Although the hard template method is commonly employed to enhance the sodium storage capacity, the reported process steps are complicated. In this study, we introduced a facile approach by utilizing ZnO as a self-sacrificed template to engineer pore structures with one step for template removal without using harmful chemicals. Our investigations reveal that pretreatment of the material before carbonization can reduce the specific surface area and defect degree of the

final hard carbon. When utilized as an anode material, the as-prepared hard carbon demonstrated a reversible capacity of 334 mAh g^{-1} at 0.05 A g^{-1} with an initial Coulombic efficiency of 84%. Even at a high current density of 2 A g^{-1} , the capacity stabilized at 183 mAh g^{-1} after 1000 continuous cycles. Electrochemical storage behavior and *ex-situ* Raman spectroscopy unveiled insights into the potential sodium storage mechanism. These findings present a new approach to enhancing the reversible properties of hard carbon anode materials for high-performance sodium-ion batteries.

1. Introduction

With the rapid development of smart grids and electric cars, the demand for lithium-ion batteries (LIBs) is growing, but concerns about limited lithium resources may hinder their further application.^[1–3] Alternatively, sodium has the benefit of being inexpensive and possessing significant reserves.^[4–6] Hard carbon materials,^[7–12] soft carbon material,^[13–17] nano-carbon material,^[18–23] alloy material,^[24–28] oxide material,^[29–31] and organic compound materials show own advantages when using in sodium-ion batteries.^[32–35] Among them, hard carbon hold great promise because of the disordered structure and large layer spacing, providing higher reversible capacity.^[36–37]

The sodium storage mechanism for hard carbon anodes in SIB is currently divided into two parts: 1) adsorption (sloping region) and 2) filling-intercalation (plateau region).^[38] The capacity provided by the slope region is typically associated with factors such as specific surface area,^[10] functional group^[39–40] and defects.^[41–42] However, a higher specific surface area with excessive functional groups and defects result in electrolyte decomposition, along with a low initial Coulombic

efficiency (ICE)^[43] and irreversible adsorption of Na^+ .^[41] Therefore, engineering hard carbon with tunable SSA, pore structures and defects by hard template strategy (including SiO_2 ,^[44] NaCl ,^[45] ZnO ^[46]) is more promising to increase the capacity with high ICE value. However, most of those hard template approaches require solvents such as HF acids or NaOH bases to remove the template, which is not convenient and environmentally unfriendly. Therefore, developing a facile approach to remove the template to engineer the porous structure of hard carbon is required but challenging.

In this study, we employ the derived ZnO from zinc gluconate as a self-sacrificed template to regulate the lattice spacing, defect degree, and SSA of hard carbons. During the carbonization process, zinc gluconate precursors and the derived ZnO are served as pore-making agents. With the increase in carbonization temperature, ZnO undergoes self-elimination, streamlining the steps involved in template removal. When utilized as an anode material, the as-prepared hard carbon (GLU-Zn10), which is derived from the precursor with the addition of 10 wt.% zinc gluconate, demonstrated a reversible capacity of 334 mAh g^{-1} at 0.05 A g^{-1} with an initial Coulombic efficiency of 84%. Even at a high current density of 2 A g^{-1} , the capacity stabilized at 183 mAh g^{-1} after 1000 continuous cycles. The electrochemical storage behavior and *ex-situ* Raman spectroscopy revealed a potential sodium storage mechanism of “adsorption-intercalation/filling.” These findings introduce a new template removal approach to improving the reversible properties of hard carbon anode materials, promising advancements in the performance of sodium-ion batteries.

[a] Z. Zhang, P. Zhao, X. Gong, J. Dai, H. Xiong, Z. Zhang, Dr. B. Wang
Shanghai Key Laboratory of Materials Protection and Advanced Materials in Electric Power, Shanghai University of Electric Power, Shanghai, 201306, China
E-mail: wangbaofeng@shiep.edu.cn

[b] G. Li, G. Liang, J. Mao, Dr. S. Zhang
School of chemical engineering, The University of Adelaide, Adelaide SA 5000 Australia
E-mail: shilin.zhang01@adelaide.edu.au

 Supporting information for this article is available on the WWW under <https://doi.org/10.1002/batt.202300552>

 © 2024 The Authors. *Batteries & Supercaps* published by Wiley-VCH GmbH. This is an open access article under the terms of the Creative Commons Attribution License, which permits use, distribution and reproduction in any medium, provided the original work is properly cited.

2. Results and Discussion

The hard carbon with engineered interlayer spacing, defect degree and varying pore size can be achieved through a

hydrothermal method, followed by controlled thermal treatment at a given temperature. In this process, the pore size can be changed by varying the amount of ZnO used as self-sacrificing agent, which is derived from the zinc gluconate during the treatment (Figure 1a and Figure S1). In Figure S2a, when pure glucose is used as precursor, from scanning electron microscope (SEM) images, we observed the formation of uniform spherical carbon structures upon carbonization at 1400 °C. However, with the addition of 5 wt.% and 10 wt.% zinc gluconate, the carbon takes on a lumpy and irregular form (Figure S2b–c). Interestingly, when the mass fraction of zinc gluconate reaches 20%, the spherical carbon structures re-emerge, indicating a reduction in the degree of disorder (Figure S2d). In Figure 1b–e, transmission electron microscopy (TEM) images further confirm the typical features of amorphous

carbon. Notably, the carbon layer spacing of GLU-Zn5 and GLU-Zn10 has the largest value at 0.394 nm and 0.392 nm, respectively, among all products (Table S1). The X-ray diffraction (XRD) patterns (Figure 2a) of all as-synthesised hard carbons indicate that no other impurities (such as ZnO template) can be found. This suggests the successful use of ZnO as a pore-forming agent for GLU-Zn, and it can be completely removed during the following process. The four samples exhibit two wide peaks around the diffraction angles of 22°~25° (002) and 43° (100), corresponding to the non-graphitized characteristics of hard carbon. Additionally, the Bragg equation was applied to calculate the average layer spacing of $d_{(002)}$ crystal planes, and the graphite-like nanocrystalline domains obtained were characterised by their thickness and average length values, namely L_c and L_a , as shown in Figure 2b and Table S1. Raman spectra

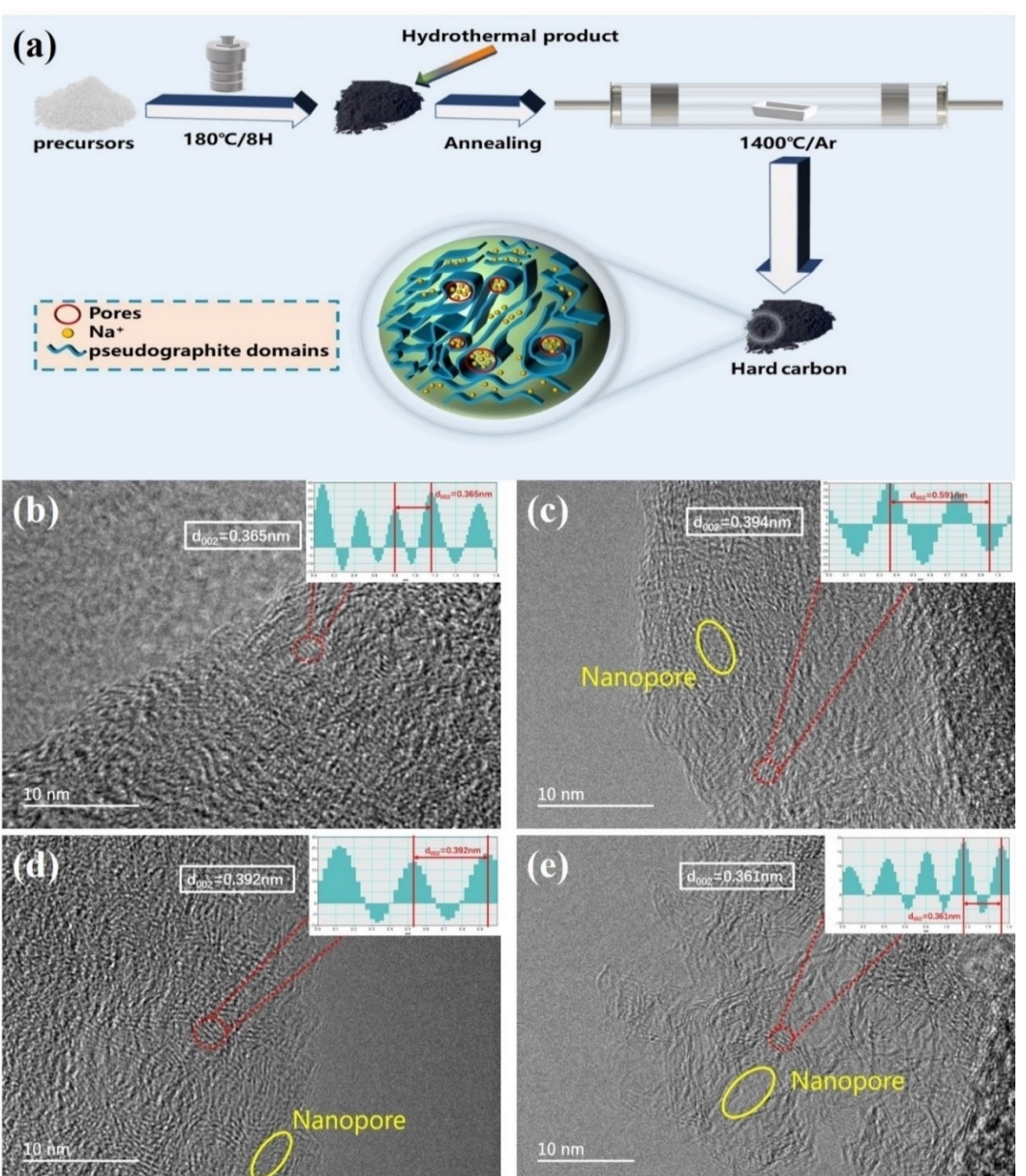


Figure 1. (a) Schematic diagram illustrating the synthesis process for GLU, GLU-Zn5, GLU-Zn10, and GLU-Zn20. TEM images of (b) GLU, (c) GLU-Zn5, (d) GLU-Zn10, and (e) GLU-Zn20. The insets of (b–e) reveal the layer spacing of the corresponding samples.

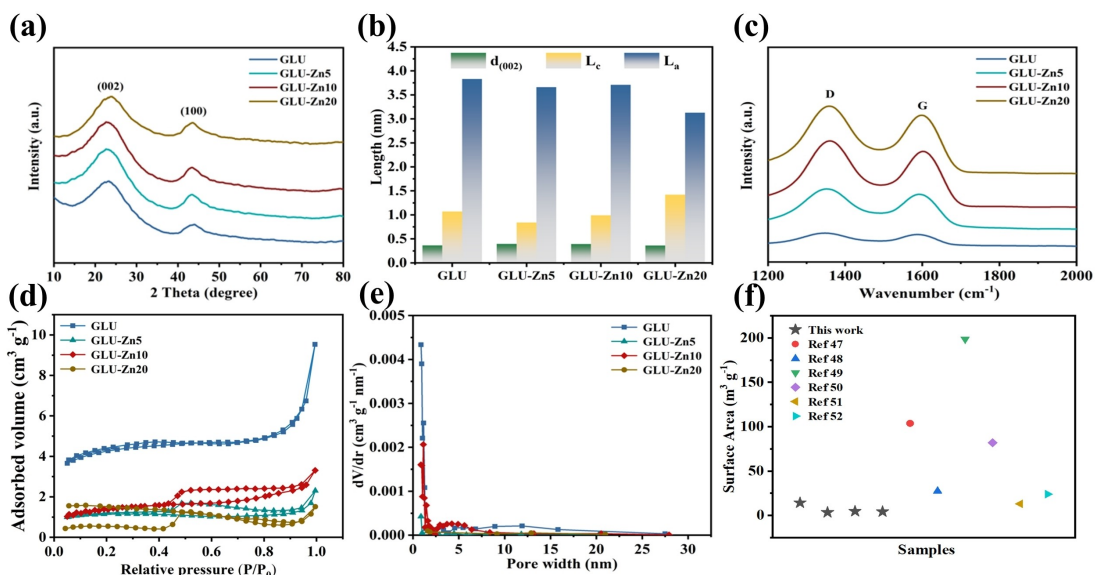


Figure 2. Structural information on GLU, GLU-Zn5, GLU-Zn10, GLU-Zn20 at 1400 °C (a) XRD patterns, (b) the variations of $d_{(002)}$, L_a and L_c (c) Raman spectrum, (d) N_2 adsorption-desorption isothermal curves and (e) pore size distribution. (f) Comparison of SSA ($m^2 g^{-1}$) with the typical carbon anodes reported previously.^[47–52]

indicate the defect degrees of the hard carbons (Figure 2c). Specifically, the I_D (disordered degree)/ I_G (graphite degree) values of GLU, GLU-Zn5, GLU-Zn10 and GLU-Zn20 were 1.007, 1.116, 1.057 and 1.012, respectively (Table S1). These values indicate that the addition of zinc gluconate correlates with a decreasing disorder degree, suggesting that higher concentrations of the additive result in a less disordered structure. In Figure 2d–e, N_2 adsorption/desorption experiments were employed for the quantitative determination of specific surface area and pore structure of our samples. Based on the type IV isotherms for all four materials, all samples exhibit a dominance of mesoporous surfaces. Furthermore, GLU has the largest specific surface area at $14.2817 m^2 g^{-1}$, while GLU-Zn5, GLU-Zn10, and GLU-Zn20 exhibit values of $3.5726 m^2 g^{-1}$, $4.6857 m^2 g^{-1}$, and $4.4029 m^2 g^{-1}$, respectively (Table S1). Compared to reported hard carbon materials, our samples consistently demonstrate relatively lower specific surface areas (Figure 2f). The lower specific surface area is conducive to inhibiting the decomposition of the electrolyte and increasing the reversibility of the cells. Furthermore, the Small Angle X-Ray Scattering (SAXS) profiles (Figure S3) display wide humps at a scattering vector (Q) of 0.1 \AA^{-1} , providing additional evidence for the existence of closed micropores.^[53] Among these samples, GLU-Zn10 has demonstrated the most abundant closed pore structure.

In order to understand the correlation between pore size and the derived ZnO agent during the treatment, we conducted substantial experiments including XRD, X-ray photoelectron spectroscopy (XPS), and TEM analysis. Figure S4a reveals distinct peaks at 31.7° , 34.4° , 36.3° , 47.6° , 56.6° , 62.9° , 66.3° , 67.9° , 69.1° , 72.7° , and 76.9° , corresponding to the (100), (002), (101), (102), (110), (103), (200), (112), (201), (004) and (202) facets of wurtzite hexagonal ZnO, respectively. As a result, we can confirm the formation of ZnO, and these ZnO particles act as templates for

pore creation during subsequent pyrolysis (as shown in the schematic diagram of ZnO as a pore-forming agent in Figure S1). The survey spectra of XPS (Figure S5) and Zn 2p spectra in Figure S4b of GLU-600 °C, GLU-Zn5-600 °C, GLU-Zn10-600 °C, and GLU-Zn20-600 °C further support this observation. These findings strongly indicate the presence of ZnO. Additionally, we observed even distribution of Zn and O elements in the corresponding EDS mappings of the pre-pyrolyzed GLU-Zn20 (Figure S6), with the size of ZnO particles matching the size of the internal pores at 1000 °C (Figure S7), and Figure S7 and Table S2 illustrated the closed pore structure changes of the chosen GLU-Zn20 at 1000–1300 °C, indicating the temperature has a key influence on pore size change. The reason why we chose GLU-Zn20 is because the change of pore size is more obvious than any other samples.

The electrochemical performances of the as-prepared GLU, GLU-Zn5, GLU-Zn10, and GLU-Zn20 samples are studied in sodium ion half cells. Figure 3a presents the constant-current charge-discharge curve of GLU, GLU-Zn5, GLU-Zn10, and GLU-Zn20 at a current density of $0.05 A g^{-1}$ for the first three cycles. Notably, the specific discharge capacity of GLU-Zn10 during the first cycle discharge reaches $397 mAhg^{-1}$, with an initial Coulombic efficiency of 84%. Additionally, Figure 3b illustrates that GLU-Zn10 materials outperform hard carbon materials reported previously in terms of ICE and initial discharge specific capacity. This confirms the feasibility of utilizing GLU-Zn10 in sodium ion batteries. Figure 3c shows the cyclic stability curve of GLU, GLU-Zn5, GLU-Zn10, and GLU-Zn20 at a current density of $0.2 A g^{-1}$. GLU-Zn10 can provide the highest capacity of $295 mAhg^{-1}$, demonstrating the superior performance among all GLU samples. Figure 3d indicates the specific discharge capacities of GLU, GLU-Zn5, GLU-Zn10, and GLU-Zn20 at 0.05 , 0.1 , 0.2 , 0.5 , 0.8 , 1 , and $2 A g^{-1}$ current densities. GLU, GLU-Zn5, and GLU-Zn10 exhibit excellent magnification performance, of

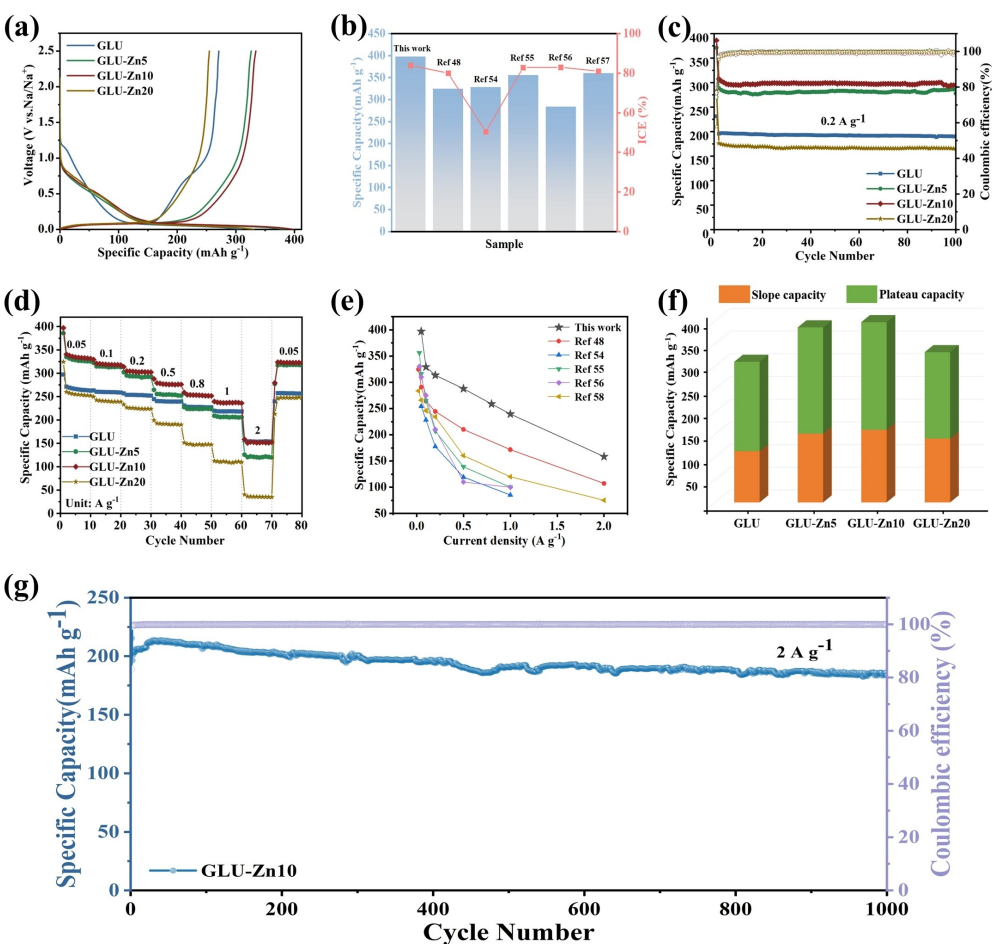


Figure 3. (a) Initial galvanostatic charge-discharge curve of GLU, GLU-Zn5, GLU-Zn10, GLU-Zn20 at 0.05 A g⁻¹. (b) Comparison of Specific capacity of initial discharge and ICE with the typical carbon anodes reported previously.^[48,54-57] (c) Cycling stability of GLU, GLU-Zn5, GLU-Zn10, GLU-Zn20 electrodes at 0.2 A g⁻¹, (d) rate properties of GLU, GLU-Zn5, GLU-Zn10, GLU-Zn20 electrodes. (e) Comparison with the rate performance of typical carbon anodes reported in the past.^[48,54-56,58] (f) Capacity of slope/plateau contribution at 0.05 A g⁻¹. (g) Long-term cycling performance of the GLU-Zn10 electrode at 2 A g⁻¹.

which GLU-Zn10 is more prominent. When the current density was recovered to 0.05 A g⁻¹, the capacity of GLU-Zn10 could be restored to 319 mAh g⁻¹. Furthermore, this material surpasses most of the selected hard carbon materials (Figure 3e). The data on slope/plateau capacity at 0.05 A g⁻¹ can be found in Figure 3f. The results clearly demonstrate the enhanced sodium storage capabilities of GLU-Zn5 and GLU-Zn10 in comparison to GLU. However, the performance of the modified GLU-Zn20 is poor, especially at high rate (Figure S8), possibly attributed to excessive pore formation due to the increased zinc gluconate, which disrupts the internal structure of the hard carbon. Concurrently, Table S1 indicates that the layer spacing of GLU-Zn20 is limiting the storage of sodium ions due to being small. In addition, Figure 3g displays the high capacity and favourable retention rate of the GLU-Zn10 anode at 2 A g⁻¹, exhibiting 183 mAh g⁻¹ after 1000 cycles.

Figure S9a-f display the CV curves of all electrodes. Notably, each electrode showed a sharp pair of redox peaks in the low voltage range (0–0.1 V). This corresponds to the Na⁺ intercalation/filling reaction. Figure S10a illustrates the CV diagram of GLU and GLU-Zn10 at 0.1 mVs⁻¹. During the first discharge, an

irreversible cathode peak occurs at 0.6 V, attributed to the generation of the SEI film. Figures S10b and S10c present the GITT profiles and calculated D_a of Na⁺. It is evident that the D_a of GLU exhibits relatively stable changes in the slope region. In contrast, the D_a changes of GLU-Zn5, GLU-Zn10, and GLU-Zn20 samples show less stability in the slope region (voltage range: 1.0–0.1 V), but they all display favorable D_a changes in the plateau region (voltage range: 0.1–0.01 V). Particularly, GLU-Zn5 and GLU-Zn10 samples exhibit a significantly improved rise rate at near 0 V voltage, potentially linked to the rapid adsorption of Na⁺ by the closed pores within the hard carbon. However, the performance of GLU-Zn20 is inferior.

To learn more about the storage process of sodium ions in GLU and GLU-Zn samples, we investigate their diffusion and pseudo-capacitance behaviors. We conducted CV curves across a scanning rate range of 0.1 to 1 mVs⁻¹ to analyze the kinetics of GLU and GLU-Zn10. Figures 4a and 4b illustrate a pair of redox peaks near 0 V, signifying that both materials are subject to diffusion control. The oxidation peak at 0.1 V further suggests the extraction of sodium ions from graphite layers or pores.^[52] As shown in Figure 4c-d, the b-values for GLU's oxidation and

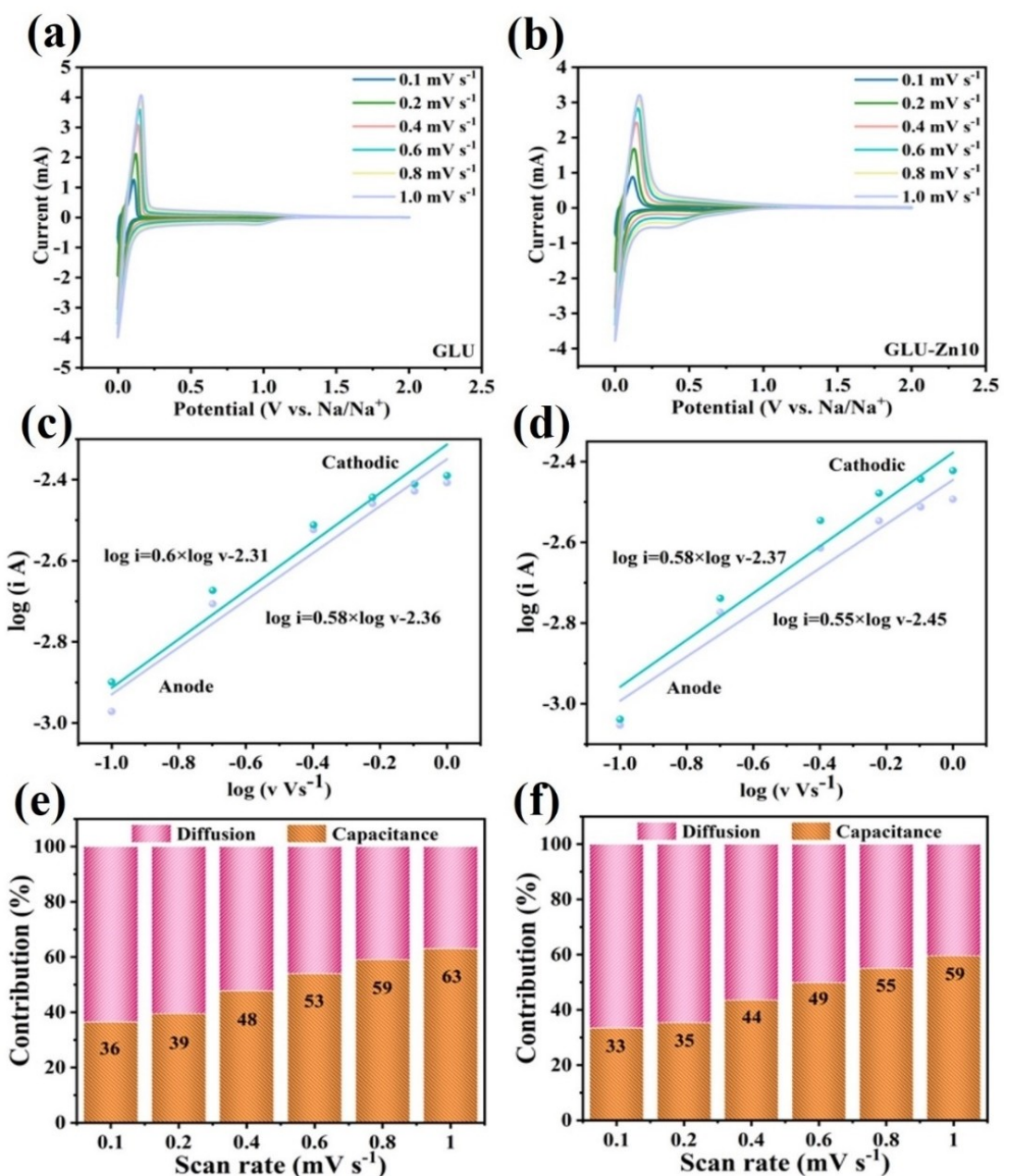


Figure 4. The CV curves at different scanning rates: (a) GLU, and (b) GLU-Zn10. Plots of log (sweep rate) versus log (current): (c) GLU, and (d) GLU-Zn10. Contribution of diffusion- and capacitive-controlled capacity of (e) GLU, and (f) GLU-Zn10 electrode at different scan rates.

reduction peaks were 0.6 and 0.58, respectively, while the *b* values for the oxidation and reduction peaks of GLU-Zn10 were 0.58 and 0.55. These findings indicate that the storage mechanism of sodium ions in GLU is primarily governed by diffusion and surface effects in the low potential platform region. Conversely, in GLU-Zn10, sodium ion storage is more susceptible to diffusion control. Additionally, we quantify the contribution of diffused and capacitive storage mechanisms. The findings revealed that as the scanning rate increased, the capacitance ratio of GLU increased from 36% to 63%, while that of GLU-Zn10 increased from 33% to 59% (Figure 4e–f). This suggests that, in contrast to GLU-Zn10, the pseudo-

capacitance is responsible for the primary contribution of the sodium storage capacity of GLU at high scanning rates. However, further testing is necessary to determine whether the diffusion mechanism of these two materials occurs within the carbon layer or in the pores.

To comprehend sodium storage, the Na⁺ storage form in Glu and GLU-Zn10 samples was analyzed using ex-situ Raman spectra. The transfer of electrons to the graphite layer during alkali metal ion insertion occupies the π* antibonding band, weakens and elongates the C–C bond, resulting in the G-band redshift.^[59] For the GLU sample (Figure 5a), the peak of the G group shifts significantly to lower frequencies when the

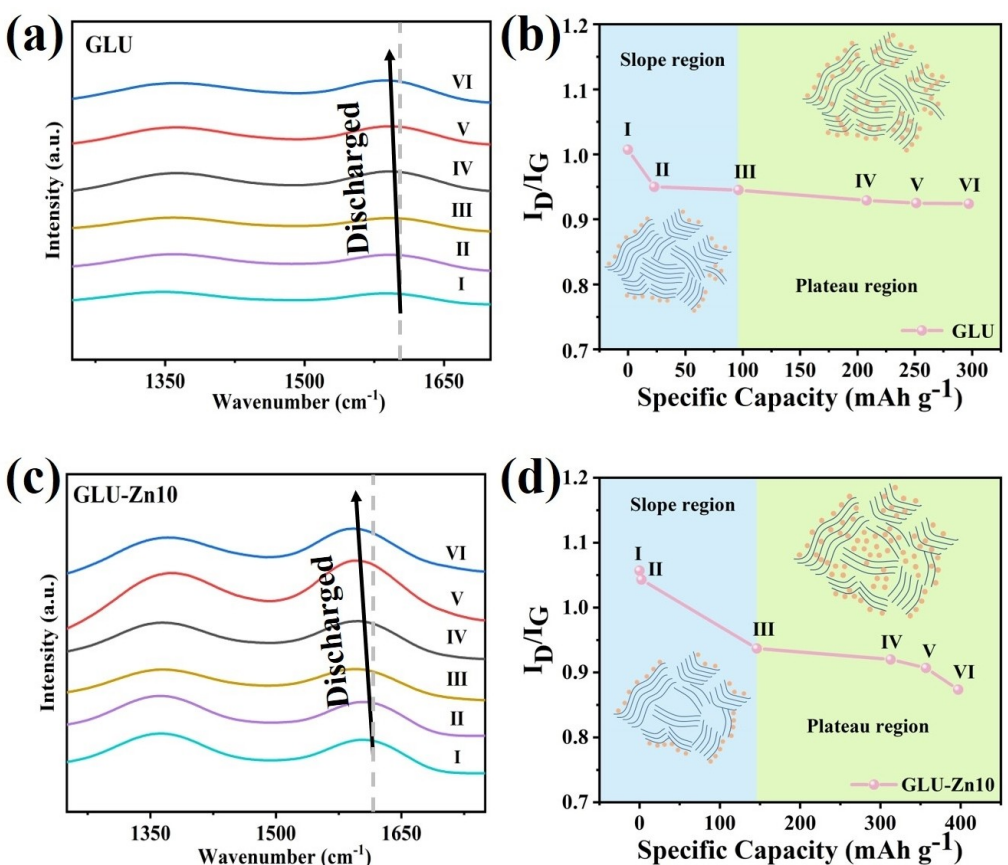


Figure 5. (a) *Ex-situ* Raman spectra are presented for GLU electrodes: I) the initial electrode, discharged to II) 0.9, III) 0.1, IV) 0.05, V) 0.035, VI) 0 V versus Na^+/Na , and (b) the evolution of I_D/I_G in relation to discharge capacity is examined. (c) *Ex-situ* Raman spectra are presented for GLU-Zn10 electrodes: I) initial electrode, discharged to II) 0.9, III) 0.1, IV) 0.05, V) 0.035, VI) 0 V versus Na^+/Na , and (d) the evolution of I_D/I_G in relation to discharge capacity is examined.

electrode potential is reduced to 0 V. This shift, from 1592 cm^{-1} to 1585 cm^{-1} , is primarily due to the intercalation of Na⁺ between graphite-like layers. Additionally, the I_D/I_G value in Figure 5b decreases from 1.007 (I) to 0.945 (III), which is attributed to the adsorption of Na⁺ at the defect site in the slope region above the potential of 0.1 V. With sodiation, it descends to 0.924 at 0 V. In Figures 5b and d, the change in the I_D/I_G ratio of the two electrodes is plotted along with the discharge capacity.

Regarding the GLU-Zn10 electrode (Figure 5c), the peak value of the G group significantly redshifts from the initial electrode (1610 cm^{-1}) to 0 V (1600 cm^{-1}), indicating that Na⁺ also contributes capacity in the GLU-Zn10 electrode through interlayer intercalation. Additionally, as shown in Figure 5d, the I_D/I_G value decreases from 1.057 to 0.937 during the initial electrode to 0.1 V, showing a more significant decline than GLU, mainly due to the greater disordered degree of GLU-Zn10. With decreasing voltage, the I_D/I_G value further decreases from 0.937 to 0.8735 during 0.1 V–0 V, indicating significant Na⁺ adsorption (or filling) in the closed pore during this period. These findings suggest that the primary means of sodium storage in the plateau region of GLU specimens is interlayer intercalation. Conversely, in GLU-Zn10 samples, the main modes of sodium

storage in the plateau region comprise interlayer intercalation as well as adsorption or filling in pores.

On the basis of the above findings, it can be deduced that the adsorption of sodium ions serves as the predominant storage mechanism for both GLU and GLU-Zn within the slope region. Interlayer intercalation is the predominant method for GLU to store sodium in the plateau region, while for GLU-Zn10, storage predominantly occurs through interlayer intercalation and closed-hole filling in the plateau region. Considering the previously calculated $d_{(002)}$ layer spacing results, the values for GLU-Zn5 and GLU-Zn10 are 0.394 nm and 0.392 nm, respectively. These substantial layer spacings confer advantages for sodium storage in the plateau region. Hence, it can be inferred that the improved sodium storage efficiency of GLU-Zn10 is associated with the larger layer spacing and the enclosed pore design.

3. Conclusions

In summary, we propose a facile template removal approach for the preparation of hard carbon, eliminating the need for traditional methods involving strong acids or bases. Both glucose and zinc gluconate undergo hydrothermal treatment,

followed by direct carbonization of the hydrothermally treated products. This process regulates the defect degree of the hard carbon and facilitates the formation of hard carbon with a small specific surface area. Compared to hard carbon produced from pure glucose as a precursor, the electrochemical performance is significantly improved. The “adsorption-intercalation/filling” mechanism of sodium storage is supported by electrochemical storage behavior and *ex-situ* Raman spectra. Our direct carbonization approach for pores structure engineering and template removal holds great promise for high-performance hard carbon anodes in sodium ion batteries.

Acknowledgements

This work is financially supported by the National Natural Science Foundation of China (No.22075173), the Science and Technology Commission of Shanghai Municipality (No.19DZ2271100 and 21010501100). S. Zhang acknowledges the financial support from the Australian Research Council (DE240100159). The authors would like to thank Dr. Yingbin Tan for his assistance and advice during the completion of the thesis. Open Access publishing facilitated by The University of Adelaide, as part of the Wiley - The University of Adelaide agreement via the Council of Australian University Librarians.

Conflict of Interests

The authors declare no conflict of interest.

Data Availability Statement

The data that support the findings of this study are available from the corresponding author upon reasonable request.

Keywords: Hard carbon • Anode • Pore-forming agent • Carbonization • Hydrothermal • Sodium-ion battery

- [1] F. Tao, Y. Liu, X. Ren, A. Jiang, H. Wei, X. Zhai, F. Wang, H.-R. Stock, S. Wen, F. Ren, *J. Alloys Compd.* **2021**, 873.
- [2] Q. Zhang, Z. Wang, S. Zhang, T. Zhou, J. Mao, Z. Guo, *Electrochim. Energy Rev.* **2018**, 1, 625.
- [3] H. Li, Q. Ma, Y. Yuan, R. Wang, Z. Wang, Q. Zhang, L. Zhang, J. Zhu, S. Zhang, J. Mao, H. Li, S. Eliseeva, V. Kondratiev, Y. Zhang, C. Zhang, Y. Wu, *Adv. Funct. Mater.* **2023**, DOI: 10.1002/adfm.202301987.
- [4] Z. Jian, S. Hwang, Z. Li, A. S. Hernandez, X. Wang, Z. Xing, D. Su, X. Ji, *Adv. Funct. Mater.* **2017**, 27.
- [5] H. Tang, M. Wang, T. Lu, L. Pan, *Ceram. Int.* **2017**, 43, 4475.
- [6] P. Bai, Y. He, X. Zou, X. Zhao, P. Xiong, Y. Xu, *Adv. Energy Mater.* **2018**, 8.
- [7] D. Zhao, H. Zhao, J. Ye, W. Song, S. Miao, H. Shen, Y. Zhao, M. Kang, Z. Li, *Electrochim. Acta* **2020**, 329.
- [8] H. Zhao, J. Ye, W. Song, D. Zhao, M. Kang, H. Shen, Z. Li, *ACS Appl. Mater. Interfaces* **2020**, 12, 6991.
- [9] *Turk. J. Chem.* **2021**, DOI: 10.3906/kim-2105-22.
- [10] D. Chen, W. Zhang, K. Luo, Y. Song, Y. Zhong, Y. Liu, G. Wang, B. Zhong, Z. Wu, X. Guo, *Energy Environ. Sci.* **2021**, 14, 2244.
- [11] S. Chen, K. Tang, F. Song, Z. Liu, N. Zhang, S. Lan, X. Xie, Z. Wu, *Nanotechnology* **2021**, 33.
- [12] A. Kamiyama, K. Kubota, D. Igarashi, Y. Youn, Y. Tateyama, H. Ando, K. Gotoh, S. Komaba, *Angew. Chem. Int. Ed. Engl.* **2021**, 60, 5114.
- [13] F. Xie, Z. Xu, A. C. S. Jensen, H. Au, Y. Lu, V. Araullo-Peters, A. J. Drew, Y.-S. Hu, M.-M. Titirici, *Adv. Funct. Mater.* **2019**, 29.
- [14] Y. Xue, M. Gao, M. Wu, D. Su, X. Guo, J. Shi, M. Duan, J. Chen, J. Zhang, Q. Kong, *ChemElectroChem* **2020**, 7, 4010.
- [15] D. Cheng, X. Zhou, H. Hu, Z. Li, J. Chen, L. Miao, X. Ye, H. Zhang, *Carbon* **2021**, 182, 758.
- [16] X.-X. He, J.-H. Zhao, W.-H. Lai, R. Li, Z. Yang, C.-M. Xu, Y. Dai, Y. Gao, X.-H. Liu, L. Li, G. Xu, Y. Qiao, S.-L. Chou, M. Wu, *ACS Appl. Mater. Interfaces* **2021**, 13, 44358.
- [17] S. Zheng, Y. Tian, W. Li, B. Wang, *ACS Appl. Mater. Interfaces* **2022**, DOI: 10.1021/acsami.2c14686.
- [18] Z. Salehpour, A. R. Mirhabibi, J. Javadpour, R. Aghababazadeh, R. Brydson, *J. Nanosci. Nanotechnol.* **2009**, 9, 4507.
- [19] J. Zhang, W. Lv, D. Zheng, Q. Liang, D.-W. Wang, F. Kang, Q.-H. Yang, *Adv. Energy Mater.* **2018**, 8.
- [20] S. Elumalai, C.-Y. Su, M. Yoshimura, *Front. Mater.* **2019**, 6.
- [21] R. Ling, S. Cai, K. Shen, Z. Sang, D. Xie, J. Sun, K. Xiong, J. Guo, X. Sun, *Ceram. Int.* **2019**, 45, 19799.
- [22] B. Wang, S. Zhang, G. Wang, H. Wang, J. Bai, *J. Colloid Interface Sci.* **2019**, 557, 216.
- [23] J. Zhou, S. Zhang, Y.-N. Zhou, W. Tang, J. Yang, C. Peng, Z. Guo, *Electrochim. Energy Rev.* **2021**, 4, 219.
- [24] N. Dang, Y. H. Wei, L. F. Hou, Y. G. Li, C. L. Guo, *Materials and Corrosion-Werkstoffe Und Korrosion* **2015**, 66, 1354.
- [25] L. O. Vogt, C. Villevieille, *J. Electrochim. Soc.* **2016**, 163, A1306.
- [26] V. P. Krasin, S. I. Soyustova, lop, presented at 11th International Conference on Mechanical Engineering, Automation and Control Systems (MEACS), Tomsk, RUSSIA, 2018.
- [27] A. G. Morachevskii, *Russ. J. Appl. Chem.* **2018**, 91, 1785.
- [28] L. Fang, N. Bahlawane, W. Sun, H. Pan, B. B. Xu, M. Yan, Y. Jiang, *Small* **2021**, 17.
- [29] T. Li, Z.-H. Long, D.-H. Zhang, *Acta Physico-Chimica Sinica* **2016**, 32, 573.
- [30] M. S. Chae, H. J. Kim, J. Lyoo, R. Attias, Y. Gofer, S.-T. Hong, D. Aurbach, *Adv. Energy Mater.* **2020**, 10.
- [31] J. Lamb, A. Manthiram, *Chem. Mater.* **2020**, 32, 8431.
- [32] H.-G. Wang, X.-B. Zhang, *Chem. - Eur. J.* **2018**, 24, 18235.
- [33] W. Zhang, P. Sun, H. Wu, S. Sun, *Comput. Mater. Sci.* **2018**, 143, 255.
- [34] L.-Y. Wang, C. Ma, X. Wei, B. Chang, K.-X. Wang, J.-S. Chen, *J. Mater. Chem. A* **2020**, 8, 8469.
- [35] A. V. Desai, D. N. Rainer, A. Pramanik, J. M. Cabanero Jr., R. E. Morris, A. R. Armstrong, *Small Methods* **2021**, 5.
- [36] J.-X. Wang, Y.-P. Zhang, Y. Guo, M.-W. Li, C.-Y. Wang, *Ionics* **2021**, 27, 677.
- [37] Y. Shi, H.-J. Li, W.-H. Bai, X.-F. Lyu, L.-J. Zhu, F. Jiang, Y.-Q. Chen, Z. Chen, *Electrochim. Acta* **2023**, 441.
- [38] X. Chen, C. Liu, Y. Fang, X. Ai, F. Zhong, H. Yang, Y. Cao, *Carbon Energy* **2022**, DOI: 10.1002/cey2.196.
- [39] F. Sun, H. Wang, Z. Qu, K. Wang, L. Wang, J. Gao, J. Gao, S. Liu, Y. Lu, *Adv. Energy Mater.* **2020**, 11.
- [40] L. Chen, L. Bai, J. Yeo, T. Wei, W. Chen, Z. Fan, *ACS Appl. Mater. Interfaces* **2020**, 12, 27499.
- [41] L. Xiao, H. Lu, Y. Fang, M. L. Sushko, Y. Cao, X. Ai, H. Yang, J. Liu, *Adv. Energy Mater.* **2018**, 8.
- [42] Y. Su, B. Johannessen, S. Zhang, Z. Chen, Q. Gu, G. Li, H. Yan, J. Y. Li, H. Y. Hu, Y. F. Zhu, S. Xu, H. Liu, S. Dou, Y. Xiao, *Adv. Mater.* **2023**, 35, e2305149.
- [43] G. Zou, H. Hou, C. W. Foster, C. E. Banks, T. Guo, Y. Jiang, Y. Zhang, X. Ji, *Adv. Sci.* **2018**, 5, 1800241.
- [44] X. Chen, Y. Fang, H. Lu, H. Li, X. Feng, W. Chen, X. Ai, H. Yang, Y. Cao, *Small* **2021**, 17, e2102248.
- [45] P. Lu, Y. Sun, H. Xiang, X. Liang, Y. Yu, *Adv. Energy Mater.* **2018**, 8.
- [46] X. Yin, Z. Lu, J. Wang, X. Feng, S. Roy, X. Liu, Y. Yang, Y. Zhao, J. Zhang, *Adv. Mater.* **2022**, 34, e2109282.
- [47] Z. Lu, J. Wang, W. Feng, X. Yin, X. Feng, S. Zhao, C. Li, R. Wang, Q. A. Huang, Y. Zhao, *Adv. Mater.* **2023**, DOI: 10.1002/adma.202211461e2211461.
- [48] Z. Hou, D. Lei, M. Jiang, Y. Gao, X. Zhang, Y. Zhang, J. G. Wang, *ACS Appl. Mater. Interfaces* **2023**, 15, 1367.
- [49] H. He, J. He, H. Yu, L. Zeng, D. Luo, C. Zhang, *Adv. Energy Mater.* **2023**, 13.
- [50] X. Chen, J. Tian, P. Li, Y. Fang, Y. Fang, X. Liang, J. Feng, J. Dong, X. Ai, H. Yang, Y. Cao, *Adv. Energy Mater.* **2022**, 12.
- [51] T. Xu, X. Qiu, X. Zhang, Y. Xia, *Chem. Eng. J.* **2023**, 452.

- [52] Q. Li, Y. Zhu, P. Zhao, C. Yuan, M. Chen, C. Wang, *Carbon* **2018**, *129*, 85.
- [53] Y. Morikawa, S.-I. Nishimura, R.-I. Hashimoto, M. Ohnuma, A. Yamada, *Adv. Energy Mater.* **2019**, *10*.
- [54] F. Wu, M. Zhang, Y. Bai, X. Wang, R. Dong, C. Wu, *ACS Appl. Mater. Interfaces* **2019**, *11*, 12554.
- [55] H. Chen, N. Sun, Q. Zhu, R. A. Soomro, B. Xu, *Adv. Sci.* **2022**, *9*, e2200023.
- [56] L. Yang, M. Hu, H. Zhang, W. Yang, R. Lv, *J. Colloid Interface Sci.* **2020**, *566*, 257.
- [57] N. Ahmad, N. Muhammad, H. Chen, J. Wang, C. Wei, M. Khan, R. Yang, *J. Colloid Interface Sci.* **2023**, *650*, 1725.
- [58] R. Xu, N. Sun, H. Zhou, X. Chang, R. A. Soomro, B. Xu, *Battery Energy* **2022**, *2*.
- [59] J. Wang, L. Yan, Q. J. Ren, L. L. Fan, F. M. Zhang, Z. Q. Shi, *Electrochim. Acta* **2018**, *291*, 188.

Manuscript received: November 24, 2023

Revised manuscript received: December 30, 2023

Accepted manuscript online: January 2, 2024

Version of record online: January 19, 2024